Journal of NUCLEAR SCIENCE and TECHNOLOGY, Vol. 45, No. 5, p. 402–422 (2008)

ARTICLE

Flow Structure of Subcooled Boiling Water Flow in a Subchannel of 3 × 3 Rod Bundles

Byong-Jo YUN[1], Goon-Cherl PARK[2], J. Enrique JULIA[3,*] and Takashi HIBIKI[4]

[1]*Korea Atomic Energy Research Institute, Taejon, 305-600, Korea*
[2]*Nuclear Engineering Department, Seoul National University, Seoul, 151-742, Korea*
[3]*Departamento de Ingeniería Mecánica y Construcción, Universitat Jaume I. Campus de Riu Sec, 12071-Castellon, Spain*
[4]*School of Nuclear Engineering, Purdue University, 400 Central Dr., West Lafayette, IN 47907-2017, USA*

(Received July 26, 2007 and accepted in revised form December 13, 2007)

In this paper, the interfacial flow structure of subcooled water boiling flow in a subchannel of 3 × 3 rod bundles is presented. The 9 rods are positioned in a quadrangular assembly with a rod diameter of 8.2 mm and a pitch distance of 16.6 mm. Local void fraction, interfacial area concentration, interfacial velocity, Sauter mean diameter, and liquid velocity have been measured using a conductivity probe and a Pitot tube in 20 locations inside one of the subchannels. A total of 53 flow conditions have been considered in the experimental dataset at atmospheric pressure conditions with a mass flow rate, heat flux, inlet temperature, and subcooled temperature ranges of 250–522 kg/m^2 s, 25–185 kW/m^2, 96.6–104.9°C, and 2–11 K, respectively. The dataset has been used to analyze the effect of the heat flux and mass flow rate on the local flow parameters. In addition, the area-averaged data integrated over the whole subchannel have been used to validate some of the distribution parameter and drift velocity constitutive equations and interfacial area concentration correlations most used in the literature.

KEYWORDS: rod bundle, subchannel, subcooled boiling flow, local measurements, drift-flux model, interfacial area concentration

I. Introduction

The subject of two-phase flow has become increasingly important in a wide variety of engineering systems for their optimum design and safe operations. Among them, the modeling of the two-phase flow in a subchannel is of great importance to the safety analysis of nuclear power plants and verification of thermal-hydraulic design codes. This fact is especially important in boiling water nuclear reactors (BWRs) since the two-phase flow is involved in its standard operational conditions. The basic structure of a two-phase flow can be characterized by two fundamental geometrical parameters such as void fraction and interfacial area concentration. The void fraction expresses the phase distribution and is a required parameter for hydrodynamic and thermal design in various industrial processes. The interfacial area describes the available area for the interfacial transfer of mass, momentum and energy, and is a required parameter for a two-fluid model formulation. Various transfer mechanisms between phases depend on the two-phase interfacial structures. Therefore, an accurate knowledge of these parameters is necessary for any two-phase flow analysis.

In view of the great importance of void fraction and interfacial area concentration for optimum system design and safe operations, extensive analytical and experimental studies have been performed. Nevertheless, local flow measurements and modeling of flow parameters in a subchannel are still limited. This is particularly true for the interfacial area concentration in subcooled boiling flow. Although some local data are available in annulus channels simulating subchannels,[1–7] very limited data on subcooled boiling flow in subchannels are available so far. In addition to this, very limited experimentally supported interfacial area models are available. In nuclear system analysis codes such as TRAC-PF1[8] and RELAP5,[9] the interfacial area concentration is calculated based on Weber number criterion and Laplace length scale, respectively. These approaches have not been verified directly by experimental data.

From this point of view, this study is intended to understand the flow structure of subcooled boiling water flow in a subchannel. To achieve it, we first make an extensive survey on existing models to predict void fraction and interfacial area concentration and on existing data in rod bundles. Then, we measure local flow parameters of subcooled boiling water flow in a subchannel of 3 × 3 rod bundles by local sensor techniques. The measured local flow parameters include void fraction, interfacial area concentration, interfacial velocity and bubble Sauter mean diameter for gas phase and liquid velocity for liquid phase. Based on the newly obtained data, we discuss the flow structure of subcooled boiling water flow in the subchannel. Finally, we evaluate existing

*Corresponding author, E-mail: bolivar@emc.uji.es

models with the newly obtained data of void fraction and interfacial area concentration, which are crucial parameters in two-phase flow analysis, and develop new empirical correlation to predict void fraction.

II. Survey of Existing Works

1. One-Dimensional Drift-Flux Models

The basic form of the one-dimensional drift-flux model is expressed by[10)]

$$\langle\langle v_g\rangle\rangle = \frac{\langle j_g\rangle}{\langle\alpha\rangle} = C_0\langle j\rangle + \langle\langle v_{gj}\rangle\rangle, \quad (1)$$

where v_g, j_g, α, C_0, j, and v_{gj} are, respectively, the gas velocity, superficial gas velocity, void fraction, distribution parameter, mixture volumetric flux, and drift velocity. $\langle\langle\ \rangle\rangle$ and $\langle\ \rangle$ indicate the void fraction weighted cross-sectional area-averaged and area-averaged quantities, respectively. The distribution parameter and void fraction weighted averaged drift velocity are defined as

$$C_0 \equiv \frac{\langle\alpha j\rangle}{\langle\alpha\rangle\langle j\rangle} \text{ and } \langle\langle v_{gj}\rangle\rangle \equiv \frac{\langle v_{gj}\alpha\rangle}{\langle\alpha\rangle} = \frac{\langle v_r(1-\alpha)\alpha\rangle}{\langle\alpha\rangle}, \quad (2)$$

where v_r is the relative velocity between phases.

As listed in **Table 1**, five different sets of constitutive equations for both C_0 and $\langle\langle v_{gj}\rangle\rangle$ have been chosen to be compared with the experimental data obtained in the subchannel of 3 × 3 rod bundles. The first 4 sets such as the constitutive equations of Bestion,[11)] Chexal *et al.*,[12)] Inoue *et al.*,[13)] and Maier and Coddington[14)] have been derived from rod bundle data (mainly differential pressure measurements) and have been successfully tested against different rod bundle databases[16)] in a wide range of void fraction conditions. The last set such as the constitutive equations of Hibiki *et al.*[15)] was derived for annulus channel geometry and obtained by local probe measurements. Table 1 provides the explicit correlations for all the constitutive equations. In what follows, brief explanations are given for all the constitutive equations.

Bestion (1990)[11)]

This correlation was developed to be used in the thermal-hydraulic code CATHARE. The correlation is based on experimental data in rod bundles with hydraulic diameters of 12 and 24 mm and also the visual observations given by Venkateswararao *et al.*[17)] The Bestion work[11)] only provides the drift velocity correlation, thus a constant distribution parameter of 1 has been assumed since it provides the most accurate results.[14)]

Chexal *et al.* (1992)[12)]

This correlation is based on the Zuber-Findlay model[10)] and the main modifications are focused on the distribution parameter. In their work, Chexal and Lellouche developed correlations for both upward and downward flows in vertical, inclined and horizontal pipes with different fluid types. In the case of upward water-steam flow in a vertical pipe, the distribution parameter and drift velocity correlations are those known as the EPRI correlation, which were developed by the same authors in 1986.[18)] In addition, the critical pressure parameter is introduced in the distribution parameter equation.

Inoue *et al.* (1993)[13)]

This correlation is also based on the Zuber-Findlay model[10)] and it was derived from void fraction data in an 8 × 8 BWR facility.[19)] An evaluation of the inlet pressure and mass flux on the distribution parameter and drift velocity is fitted with the experimental data.

Maier and Coddington (1997)[14)]

This correlation was developed using the same approach as the Inoue *et al.* correlation,[13)] but more experimental conditions and flow configurations have been used for the correlation fitting.[14)]

Hibiki *et al.* (2003)[15)]

This correlation modifies the distribution parameter for subcooled boiling flow obtained by Ishii[20)] in order to be used in annulus geometry. The modification is performed using the bubble layer thickness formulation[15)] and local flow experimental data obtained in the annulus with inner and rod diameters of 38.1 and 19.1 mm, respectively. This formulation is only valid for bubbly flow conditions. The drift velocity correlation is the one developed by Ishii.[20)]

2. Interfacial Area Concentration Models

As listed in **Table 2**, five different sets of constitutive equations for interfacial area concentration have been chosen to be compared with the experimental data obtained in the subchannel of 3 × 3 rod bundles. The constitutive equation of Zeitoun *et al.*[21)] has been developed from annulus data, and the constitutive equations of Hibiki and Ishii[22)] and Hibiki *et al.*[23)] have been derived mainly from round pipe and annulus data since there is no experimental database on interfacial area concentration of boiling flow in rod bundle geometry. The last two sets are currently utilized in system analysis codes such as TRAC-PF1[8)] and RELAP5.[9)] The reduced forms of TRAC-PF1 and RELAP5 correlations, which can be applicable to the bubbly flow regime, are presented in Table 2. Table 2 provides the explicit formulations of all the correlations. In what follows, brief explanations are given for all the constitutive equations.

Zeitoun *et al.* (1994)[21)]

In this correlation, the nondimensional interfacial area concentration, N_{a_i}, is correlated with the void fraction and Reynolds number, N_{Re_i}. The nondimensional parameters are defined as

$$N_{a_i} \equiv \langle a_i\rangle Lo \text{ and } N_{Re_i} \equiv \frac{G}{\langle a_i\rangle\mu_f}, \quad (3)$$

where a_i, G, and μ_f are, respectively, the interfacial area concentration, mass velocity, and liquid viscosity. Laplace length, Lo, is defined as

$$Lo \equiv \sqrt{\frac{\sigma}{g\Delta\rho}}, \quad (4)$$

where σ, g, and $\Delta\rho$ are, respectively, the surface tension, gravitational acceleration, and density difference between phases.

Hibiki and Ishii (2002)[22)]

This correlation was developed based on the simplification of the interfacial area transport equation. The important

Table 1 Existing drift flux models applicable to bundle or subchannel test sections

Authors	C_0 expression	$\langle\langle v_{gj}\rangle\rangle$ expression	Applicable range	Ref.
Bestion (1990)	$C_0 = 1$	$\langle\langle v_{gj}\rangle\rangle = 0.188\sqrt{\frac{gD_H\Delta\rho}{\rho_g}}$	Whole range	11)
Chexal *et al.* (1992)	$C_0 = \frac{L}{K_0 + (1-K_0)\alpha^r}$ $L = \frac{1-e^{-C_1\alpha}}{1-e^{-C_1}}, \quad C_1 = \frac{4p_{crit}^2}{p(p_{crit}-p)}$ $K_0 = B_1 + (1-B_1)\left(\frac{\rho_g}{\rho_f}\right)^{1/4}, \quad r = \frac{1+1.57\left(\frac{\rho_g}{\rho_f}\right)}{1-B_1}$ $B_1 = min\left(0.8, \frac{1}{1+e^{-Re/60000}}\right), \quad Re = max(Re_f, Re_g)$	$\langle\langle v_{gj}\rangle\rangle = 1.41\left(\frac{g\sigma\Delta\rho}{\rho_f^2}\right)^{1/4} C_2C_3C_4C_9$ $C_2 = \begin{cases} 0.4757\left(ln\left(\frac{\rho_f}{\rho_g}\right)\right)^{0.7} & if\ \frac{\rho_f}{\rho_g} \le 18 \\ \begin{cases} 1 & if\ C_5 \ge 1 \\ \left(1-exp\left(\frac{-C_5}{1-C_5}\right)\right)^{-1} & if\ C_5 < 1 \end{cases} & if\ \frac{\rho_f}{\rho_g} > 18 \end{cases}$ $C_3 = max\left(0.5, 2exp\left(\frac{-\lvert Re_f\rvert}{60000}\right)\right); \quad C_4 = \begin{cases} 1 & if\ C_7 \ge 1 \\ \left(1-exp\left(\frac{-C_7}{1-C_7}\right)\right)^{-1} & if\ C_7 < 1 \end{cases}$ $C_5 = \sqrt{150\frac{\rho_g}{\rho_f}}, \quad C_7 = \left(\frac{0.09144}{D_H}\right)^{0.6}, \quad C_9 = (1-\alpha)^{B_1}$	Whole range	12)
Inoue *et al.* (1993)	$C_0 = 6.76\times10^{-3}p + 1.026$	$\langle\langle v_{gj}\rangle\rangle = (5.1\times10^{-3}G + 6.91\times10^{-2})\times(9.41\times10^{-2}p^2 - 1.99p + 12.6)$	Whole range	13)
Maier and Coddington (1997)	$C_0 = 2.57\times10^{-3}p + 1.0062$	$\langle\langle v_{gj}\rangle\rangle = (6.73\times10^{-7}p^2 - 8.81\times10^{-5}p + 1.05\times10^{-3})G +$ $(5.63\times10^{-3}p^2 - 1.23\times10^{-1}p + 0.8)$	Whole range	14)
Hibiki *et al.* (2003)	$C_0 = \left(1.2 - 0.2\sqrt{\frac{\rho_g}{\rho_f}}\right)\left(1-e^{-3.12\langle\alpha\rangle^{0.212}}\right)$	$\langle\langle v_{gj}\rangle\rangle = \sqrt{2}\left(\frac{g\sigma\Delta\rho}{\rho_f^2}\right)^{1/4}(1-\langle\alpha\rangle)^{1.75}$	Bubbly flow	15)
Present work	$C_0 = \left(1.05 - 0.05\sqrt{\frac{\rho_g}{\rho_f}}\right)\left(1-e^{-2.92\langle\alpha\rangle^{0.146}}\right)$	$\langle\langle v_{gj}\rangle\rangle = \sqrt{2}\left(\frac{g\sigma\Delta\rho}{\rho_f^2}\right)^{1/4}(1-\langle\alpha\rangle)^{1.75}$	Bubbly flow	

Table 2 Existing interfacial area concentration models applicable to annulus geometry under boiling flow conditions

Authors	IAC correlation	Applicable range	Ref.
Zeitoun *et al.* (1994)	$\langle a_i \rangle = 3.24\left(\frac{\sigma}{g\Delta\rho}\right)^{-0.55}\alpha^{0.757}\left(\frac{G}{\mu_f}\right)^{-0.1}$	Bubbly flow	21)
Hibiki and Ishii (2002)	$\langle a_i \rangle = 3.02\left(\frac{\sigma}{g\Delta\rho}\right)^{-0.174}\alpha\frac{\langle\varepsilon\rangle^{0.0796}}{\upsilon_f{}^{0.239}D_H{}^{0.335}}$ $\langle\varepsilon\rangle = g\lvert\langle j_g\rangle\rvert exp(-0.0005839\,Re_f) + \frac{\lvert\langle j\rangle\rvert}{\rho_m}\left(\frac{-dp}{dz}\right)_F\{1 - exp(-0.0005839N_{Re_f})\}$ $Re_f = \frac{\langle j_f\rangle D_H}{\upsilon_f}$	Bubbly flow	22)
Hibiki *et al.* (2006)	$\langle a_i \rangle = 3.68\left(\frac{\sigma}{g\Delta\rho}\right)^{-0.174}\alpha^{0.83}\frac{\langle\varepsilon\rangle^{0.0796}}{\upsilon_f{}^{0.239}D_H{}^{0.335}}\left(\frac{\rho_f}{\rho_g}\right)^{-0.138}$ $\langle\varepsilon\rangle = g\lvert\langle j_g\rangle\rvert exp(-0.0005839\,Re_f) + \frac{\lvert\langle j\rangle\rvert}{\rho_m}\left(\frac{-dp}{dz}\right)_F\{1 - exp(-0.0005839N_{Re_f})\}$ $Re_f = \frac{\langle j_f\rangle D_H}{\upsilon_f}$	Bubbly flow	23)
TRAC-PF1 (1993)	$\langle a_i \rangle = \frac{6\langle\alpha\rangle}{\langle D_{Sm}\rangle}$ $\langle D_{Sm}\rangle = 2\sqrt{\frac{\sigma}{g\Delta\rho}}$	Reduced form for bubbly flow	8)
RELAP5 (1995)	$\langle a_i \rangle = \frac{3.6\langle\alpha\rangle}{\langle D_0\rangle}$ $\langle D_0\rangle = \frac{1}{2}\frac{10\sigma}{\rho_f\langle v_r\rangle^2};\quad \langle v_r\rangle = C_1\langle\langle v_g\rangle\rangle - C_0\langle\langle v_f\rangle\rangle;\quad C_1 = \frac{1 - C_0\langle\alpha\rangle}{1 - \langle\alpha\rangle}$	Reduced form for bubbly flow	9)

parameters that govern the interfacial area concentration are obtained by physical considerations and they are the void fraction, bubble Reynolds number, and Laplace length. The bubble Reynolds number, Re_b is defined as

$$Re_b \equiv \frac{\langle\varepsilon\rangle^{1/3}Lo^{4/3}}{\nu_f} \tag{5}$$

where ν_f is the kinematic viscosity of the liquid phase and ε is the energy dissipation.

Hibiki *et al.* (2006)[23)]

This correlation was developed based on the simplification of the interfacial area transport equation with special considerations for the boiling bubbly flow, and two versions of the correlation are given, the first one developed for atmospheric pressure conditions and the second one that considers the pressure effects. In the atmospheric pressure correlation, the important parameters are the same as considered by Hibiki and Ishii (2002).[22)] In the second correlation, the pressure effect is considered through the density ratio, N_ρ as

$$N_\rho \equiv \frac{\rho_f}{\rho_g} \tag{6}$$

The experiments of the present work were performed under ambient pressure conditions, so both correlations provide similar results and only the one that takes pressure effects into account will be considered.

TRAC-PF1(1993)[8)]

In the system analysis code TRAC-PF1, the interfacial area concentration is calculated from the void fraction and Sauter mean diameter, D_{Sm}. The Sauter mean diameter is calculated from the Laplace length.

RELAP5(1995)[9)]

In the system analysis code RELAP5, the interfacial area concentration is calculated from the void fraction and a characteristic bubble diameter, D_0. The characteristic bubble diameter is calculated from the critical Weber number.

3. Experimental Databases

The existing experimental datasets in rod bundle geometry only provide void fraction data. In most of the published works, the void fraction measurements were performed using differential pressure transducers. In some cases, more sophisticated techniques such as X-ray tomography[19,24)] and γ densitometry[25)] were used. Very limited local data of void fraction and interfacial area concentration are available for boiling flow in rod bundle geometry. A detailed list of the experimental datasets is given in **Table 3**. The experimental facilities used comprise a wide range of rod bundle geometries and dimensions, from the quasi-real-sized LSFT (with 1008 heated rods) to the simplified TPTF (with only 24 heated rods), and flow conditions.

Table 3 Existing databases obtained in bundle or subchannel test section

Experimental facility	Type	Length [m]	Rods (heated)	D_H [mm]	d_r [mm]	Axial power distribution	ΔT_{sub} [K]	p [Mpa]	G [Kg/m^2 s]	q [kW m^{-2}]	No. flow cond.	Measured parameters	Measurement technique	Ref.
PERICLES (1985)	PWR	3.7	357 (357)	9.5	11	Chopped cosine	20/60	0.3–0.6	21–48	11–40	21	$\langle\alpha\rangle$	DP transducers	26)
NEPTUN (1988)	LWHCR	1.7	37 (37)	10.7	4	Chopped cosine	0.5/3	0.4	42/91	5/10	48	$\langle\alpha\rangle$	DP transducers	27)
BWR 4 × 4 (1990)	BWR	3.7	16 (16)	12.3	12	Uniform	0	0.5/1	833/1390	350–743	20	$\langle\alpha\rangle$	X ray tomography	24)
BWR 8 × 8 (1991)	BWR	3.7	64 (62)	12.3	13	Uniform/ Chopped cosine	9–12	1–8.6	284–1988	225–3377	20	$\langle\alpha\rangle$	DP transducers and X ray tomography	19)
LSTF (1990)	PWR	3.7	1104 (1008)	9.5	13	Chopped cosine	0	1/7.3/15	2.2–84	5–45	14	$\langle\alpha\rangle$	DP transducers	28)
TPTF (1994)	PWR	3.7	32 (24)	9.5	10	Uniform	5–35	3/6.9/11.8	11–189	9–170	18	$\langle\alpha\rangle$	γ radiation and dP transducerD	25)
THTF (1982)	PWR	3.7	64 (60)	9.5	11	Uniform	46–118	3.9–8.1	3.1–29	11–74	11	$\langle\alpha\rangle$	DP transducers	29)
Present work	BWR	1.7	9 (9)	18.6	8.2	Uniform	2–11	0.12	250–522	25–185	53	$\alpha, a_i, v_g, D_{Sm}, v_f$	Conductivity probe, pitot tube	

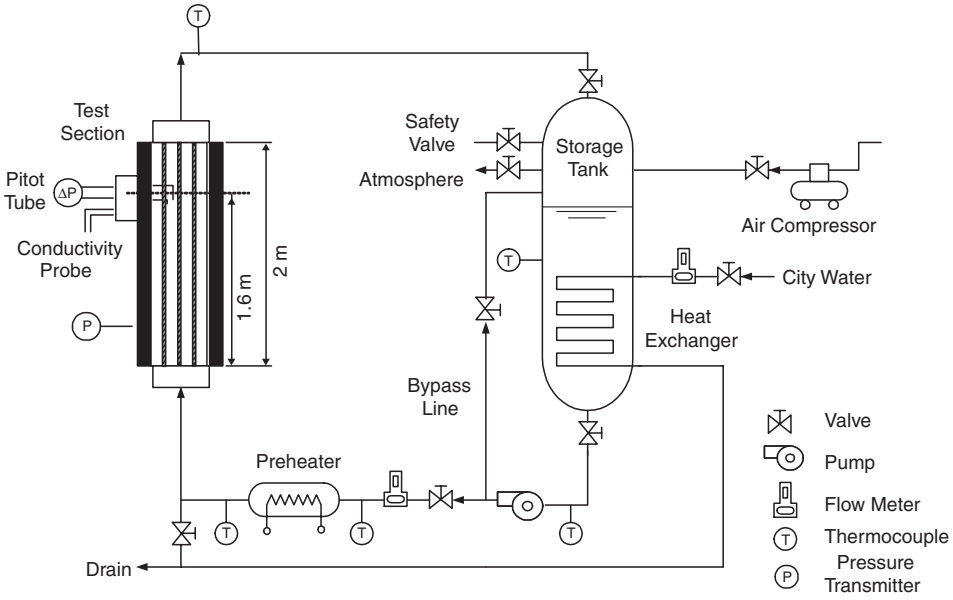

Fig. 1 Schematic diagram of the flow loop

III. Experimental Setup and Methodology

1. Steam–Water Boiling Loop

Figure 1 shows a schematic diagram of the SNU (Seoul National University) steam-water boiling loop used in the experiments. The test facility consists of a stainless steel pump, a preheater, a by-pass line, a flow metering system, a pressurizer system, a secondary heat removal system, and a storage tank. The heat exchange system allows working with a subcooling temperature range, ΔT_{sub}, between 2 and 11 K. Distilled water was used as a coolant in a closed loop. The water flow rate is measured using a conner-tap orifice plate flowmeter with an accuracy of ±4.5%. The mass flow rate range is between 250 and 522 kg/(m^2 s). The test section is composed of a 49.8 × 49.8 mm cross section, 2,000-mm-high channel. **Figure 2**a depicts the cross-sectional view of the test channel and it is composed of a squared lattice of 3 × 3 heating rods of 8.2 mm diameter. The maximum heating power of each rod is 185 kW/m^2. The hydraulic diameter of the system, D_H, is 18.6 or 34.6 mm depending if the complete rod bundle (including the 9 rods and the outer channel walls) or only the measured subchannel sections are considered, respectively. The local probes are located 1.6 m downstream of the inlet of the test channel ($z/D_H = 46$ for $D_H = 34.6$ mm (subchannel-based hydraulic diameter) or $z/D_H = 86$ for $D_H = 18.6$ mm (whole-bundle-based hydraulic diameter)). A traversing system is used to displace the probes inside the test section. Figure 2b shows the coordinates of the local two-phase flow measurement positions for every flow condition. All the experiments were performed in a bubbly flow regime at an inlet pressure of 0.12 MPa. The detailed experimental conditions are tabulated in **Table 4**.

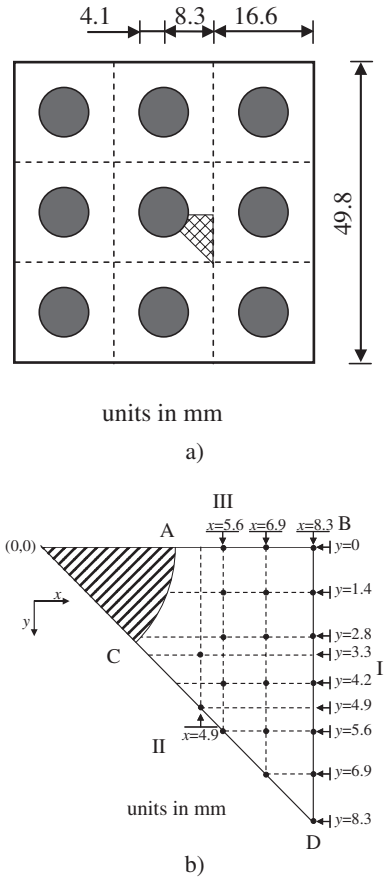

Fig. 2 a) Cross-sectional view of the subchannel test section, b) probe locations inside the subchannel

2. Conductivity Probe

Local vapor phase measurements were performed with a double sensor conductivity probe, which is applicable to the bubbly flow regime. Void fraction, interfacial area concentration, interfacial velocity, and bubble Sauter mean diameter have been measured. The details of the double-sensor conductivity probe measurements can be found in the literature.[2,30] The acquisition sampling frequency varied between

Table 4 One-dimensional data (sorted by G value)

G [kg/m^2 s]	T_{in} (C)	ΔT_{sub} (C)	q [kW/m^2]	$\langle j_g \rangle$ [m/s]	$\langle j_f \rangle$ [m/s]	$\langle \alpha \rangle$ [-]	$\langle a_i \rangle$ [m^{-1}]	C_0 [-]	$\langle\langle v_{gj} \rangle\rangle$ [m/s]
250	102.4	5.0	71.0	0.051	0.261	0.110	222	0.95	0.15
265	104.1	2.8	61.4	0.041	0.276	0.089	213	0.94	0.15
266	102.0	10.0	56.17	0.010	0.277	0.032	125	0.90	0.14
274	101.9	10.4	25.0	0.017	0.286	0.046	159	0.91	0.21
274	101.7	10.7	39.0	0.024	0.286	0.066	203	0.93	0.20
275	101.6	10.9	28.5	0.070	0.287	0.159	339	0.96	0.12
276	103.8	8.2	39.8	0.034	0.288	0.089	252	0.93	0.17
282	103.2	3.5	47.2	0.023	0.295	0.060	195	0.93	0.18
284	102.1	4.8	31.6	0.014	0.296	0.040	141	0.91	0.22
284	101.5	10.	42.5	0.006	0.297	0.018	59	0.87	0.21
288	101.4	5.6	25.0	0.011	0.301	0.027	109	0.92	0.23
304	103.7	3.2	56.2	0.028	0.317	0.076	206	0.93	0.14
307	102.2	4.5	56.2	0.018	0.320	0.051	145	0.88	0.21
312	103.0	3.7	39.0	0.020	0.326	0.049	161	0.93	0.13
317	101.9	5.1	87.8	0.022	0.331	0.055	137	0.89	0.19
317	96.7	10.8	56.2	0.036	0.331	0.088	249	0.96	0.16
322	102.7	4.5	132.8	0.056	0.336	0.112	210	0.93	0.19
323	102.6	4.8	120.8	0.016	0.337	0.039	120	0.89	0.21
324	101.4	5.6	76.5	0.014	0.338	0.037	127	0.88	0.20
325	103.6	3.3	140.8	0.011	0.340	0.027	105	0.87	0.21
327	101.8	5.4	140.8	0.052	0.342	0.100	200	0.97	0.20
328	102.1	5.3	43.4	0.010	0.342	0.025	90	0.88	0.22
332	101.5	5.2	45.5	0.027	0.346	0.067	174	0.90	0.19
332	103.7	3.7	151.4	0.027	0.347	0.067	169	0.89	0.17
334	96.6	10.4	65.9	0.064	0.349	0.134	303	0.98	0.18
335	101.7	5.8	120.8	0.034	0.349	0.076	165	0.91	0.20
337	105.2	2.5	110.0	0.024	0.352	0.063	173	0.89	0.18
339	103.4	5.0	25.0	0.039	0.354	0.082	190	0.91	0.18
352	104.1	2.8	103.5	0.024	0.367	0.048	134	0.87	0.16
354	103.4	4.0	110.0	0.071	0.369	0.134	235	0.93	0.18
354	104.9	2.0	119.4	0.035	0.369	0.075	223	0.90	0.14
354	102.5	4.5	158.4	0.041	0.370	0.093	192	0.91	0.18
355	101.6	4.8	119.4	0.008	0.369	0.020	75	0.81	0.17
357	102.1	3.8	76.5	0.011	0.373	0.027	95	0.83	0.14
358	103.8	3.2	172.0	0.040	0.373	0.084	183	0.88	0.14
361	102.3	4.9	132.8	0.009	0.376	0.022	100	0.88	0.21
361	103.6	3.1	137.9	0.019	0.376	0.049	152	0.89	0.18
361	103.4	3.0	146.1	0.083	0.377	0.150	327	0.95	0.19
361	104.2	2.5	99.9	0.014	0.377	0.032	107	0.86	0.14
364	103.6	3.6	33.4	0.006	0.380	0.015	56	0.83	0.23
365	102.8	4.1	139.3	0.053	0.380	0.106	204	0.93	0.17
372	102.4	3.9	76.5	0.034	0.389	0.071	162	0.88	0.16
377	102.6	4.3	93.1	0.049	0.394	0.108	306	0.93	0.17
411	103.2	3.7	158.4	0.020	0.429	0.040	103	0.86	0.19
482	101.8	5.1	144.5	0.010	0.503	0.023	71	0.83	0.20
490	102.9	3.8	147.6	0.014	0.511	0.035	100	0.84	0.18
503	103.7	4.0	185.4	0.060	0.525	0.130	393	0.89	0.08
506	104.1	4.8	172.0	0.021	0.528	0.047	126	0.84	0.15
506	104.3	3.8	172.0	0.016	0.528	0.034	99	0.83	0.14
512	103.8	4.3	185.4	0.023	0.535	0.052	138	0.84	0.13
513	102.9	3.8	141.6	0.018	0.535	0.039	106	0.83	0.16
513	103.4	4.4	158.4	0.012	0.535	0.028	84	0.80	0.13
522	102.7	3.4	171.2	0.034	0.545	0.079	261	0.83	0.10

25 and 40 kHz depending on the flow conditions.

The accuracy of the double-sensor conductivity probe method has been checked in air-water benchmark experiments in an 8-mm-diameter acrylic pipe.[2)] The flow conditions of the test loop in the benchmark experiment are $0.5\,\mathrm{m/s} \leq \langle j_f \rangle \leq 3\,\mathrm{m/s}$ and $0.02 \leq \langle \alpha \rangle \leq 0.42$. The void fraction measured using the conductivity probe has been checked with entrapped air volume and the maximum rela-

tive error has been estimated to be 10%. The bubble interfacial velocity has been checked using a high-speed CCD camera (1,000 frames per second) obtaining a maximum relative error of 5% under all the flow conditions. The interfacial area concentration has been computed from the bubble frequency and bubble interface velocity. The comparison with a photographic method indicated that the measurement accuracy of the interfacial area concentration was of the same order as the measurement accuracy of the bubble interface velocity,[31] namely ±6.95%.

3. Pitot Tube

The local liquid velocity has been obtained using a calibrated Pitot tube (diameter of 1.6 mm). This system includes a differential pressure transducer and a cold water injection system in order to avoid the vapor phase entrapment. The local liquid velocity is calculated using the Bosio and Malnes model.[32]

The accuracy of the Pitot tube results has been checked in single-phase and air-water experiments under similar flow conditions as in the conductivity probe measurements. The cross-sectional integrated liquid velocity measured using the Pitot tube has been compared with the area-averaged liquid velocity measured using the flowmeter. A maximum relative error under all the flow conditions has been estimated to be below 5%.[2]

IV. Results and Discussion

1. Local Flow Parameters

In order to obtain a general view of the local flow parameter distributions in the subchannel, two sets of 3D plots are shown in **Figs. 3** and **4**. The information is displayed by grouping the graphs in two different sets (one for each figure). In this way, the effect of the mass flow rate and the heat flux on the two-phase flow local parameters can be studied. These two working parameters, heat flux and mass flow rate, have been chosen since they are easily controllable in the experimental setup. The 3D plots have been obtained from the local data points shown in Fig. 2b and the mesh has been created from linear interpolation between the data points. Due to the finite size of the conductivity probe and Pitot tube, measurements were impossible close to the rod. With the aim of facilitating the acquisition of visual information, the mesh has been mirrored using the diagonal of the subchannel as a mirroring axis and the rod surface has been included. In both graphs, the void fraction, α, interfacial area concentration, a_i, bubble interfacial velocity, v_g, liquid velocity, v_f, and bubble Sauter mean diameter, D_{Sm}, are shown for different flow conditions.

In Fig. 3, the effect of the increment in the heat flux, q, with a constant mass flow rate, G, is shown. The values of inlet temperature, T_{in}, and liquid subcooling, ΔT_{sub}, are kept constant. It is possible to observe a bubble (or void) layer around the rod surface where the bubble-related parameter values are more significant. An increment in the heat flux of the heater rod produces an increment in the void fraction layer peak value and thickness around the rod surface. The maximum void fraction peak value is around 0.3 and the maximum bubble (or void) layer thickness occupies 80% of the subchannel cross-sectional area. An increment in the heat flux of the heater rod also produces an increment in the interfacial area concentration. The interfacial area concentration shows a trend similar to the void fraction, since the interfacial area concentration is approximately proportional to the void fraction in the bubbly flow regime. In addition, the interfacial velocity shows a 30% increment for the evaluated q range and it has a similar value in all the subchannels. The liquid velocity is not affected by the increment in the q value. That means that the change in the liquid velocity produced by the density change near the rod surface is not significant compared with the bulk liquid velocity or that this effect is located very near the rod. The Sauter mean diameter is greatly increased with the q values, ranging from 2 to 6 mm. For low q values, the maximum D_{Sm} occurs near the rod; however, when the heat flux is incremented, the D_{Sm} shows a maximum in the center of the subchannel.

In Fig. 4, the effect of the increment in the mass flow rate, G, with a constant heat flux, q, is shown. The values of T_{in} and ΔT_{sub} are kept constant. An increment in the G value corresponds to a decrement in the void fraction layer thickness around the rod surface, but not in the void fraction layer peak. The interfacial area concentration shows a similar trend, but also a peak value reduction is observed. In addition, the interfacial and liquid velocities show a similar value in all the subchannels, with a slight decrease in the interfacial velocity with the mass flow rate. The Sauter mean diameter is greatly reduced with the G values. For low G values, the maximum D_{Sm} occurs in the center of the subchannel; however, when the mass flow rate is incremented, the D_{Sm} shows a maximum near the rod.

Figures 5 to **9** show local data of the void fraction, interfacial area concentration, interfacial velocity, liquid velocity, and Sauter mean diameter, respectively, for the flow conditions shown in **Table 5**. In this way, the effects of q and G in the local flow values can be analysed (q effect in the same graph and G effect in the comparison between graphs in the same row). Three different profiles are shown for every flow condition. The upper, middle, and lower figures, respectively, correspond to profiles along the y-axis (Profile I), diagonal (r) axis (Profile II), and x-axis (Profile III) in Fig. 2b. Normalized coordinates have been used, P_0 and R_0 being the pitch of the bundle and the rod radius, respectively. In the Profile I, zero and unity in the abscissa correspond to the points B and D, respectively, in Fig. 2b. In the Profile II, zero and unity in the abscissa correspond to the points C and D, respectively, in Fig. 2b. In the Profile III, zero and unity in the abscissa correspond to the points A and B, respectively, in Fig. 2b.

As can be seen from the Profile I (upper figure) in Fig. 5, the void fraction change along the y-axis is less significant due to remote measuring points from the heater rods but the void fraction near the heater rods ($y/(P_0/2) \lesssim 0.5$) tends to be higher. The void fraction change along the x-axis (see Profile III (lower figure)) is more pronounced than that along the r-axis (see Profile II (middle figure)) since the channel gap in the x-direction is smaller than that in the r-direction. The void fraction has a single peak near the heater rod and

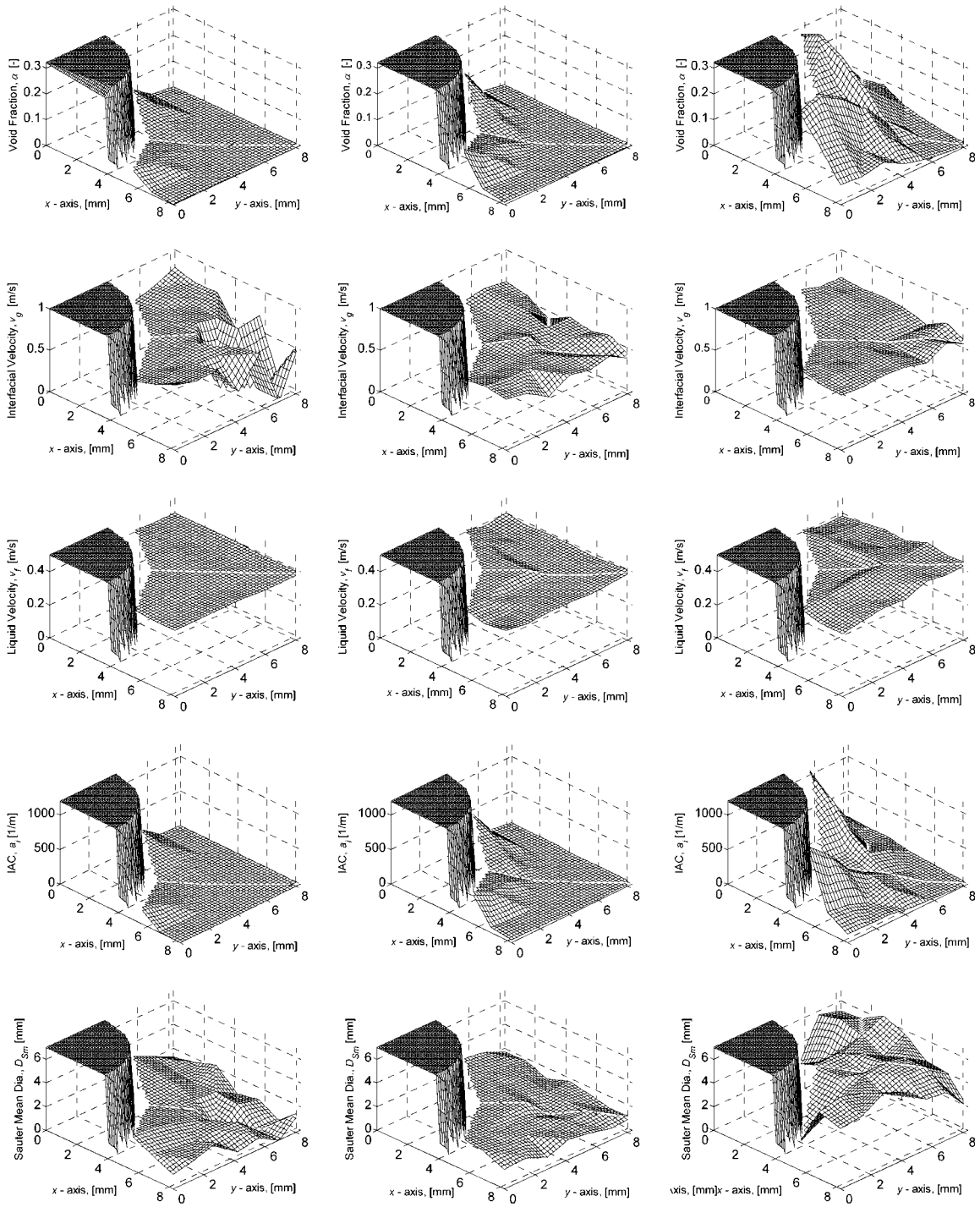

Fig. 3 Evolution of two-phase flow parameters with q. First column: $G = 339\,\mathrm{kg/m^2\,s}$, $q = 25.0\,\mathrm{kW/m^2}$, $T_{in} = 103.4^\circ\mathrm{C}$, $\Delta T_{sub} = 5.0^\circ\mathrm{C}$; second column: $G = 317\,\mathrm{kg/m^2\,s}$, $q = 56.2\,\mathrm{kW/m^2}$, $T_{in} = 101.9^\circ\mathrm{C}$, $\Delta T_{sub} = 5.1^\circ\mathrm{C}$; third column: $G = 354\,\mathrm{kg/m^2\,s}$, $q = 158\,\mathrm{kW/m^2}$, $T_{in} = 102.5^\circ\mathrm{C}$, $\Delta T_{sub} = 4.5^\circ\mathrm{C}$

decreases toward the channel center (point D in Fig. 2b). As shown in Fig. 6, the interfacial area concentration distribution is quite similar to the void fraction distribution, since the interfacial area concentration is approximately proportional to the void fraction in the bubbly flow regime. Figures 7 and 8 show the distributions of interfacial and liquid velocities over the subchannel. The velocity distributions in the measured plane are more or less uniform. The bubble Sauter mean diameter tends to decrease around the channel center due to relatively high subcooling near the channel center.

As observed in Figs. 3 and 4, the increment in the heat flux in the rod with a constant value of mass flow rate produces an increment in the void fraction layer peak value and thickness. The maximum void fraction peak value is around 0.3 and the bubble layer thickness value goes from 0.5 to 1. The large values of the bubble layer thickness are due to the high inlet temperature ($\sim$102°C). The dependence

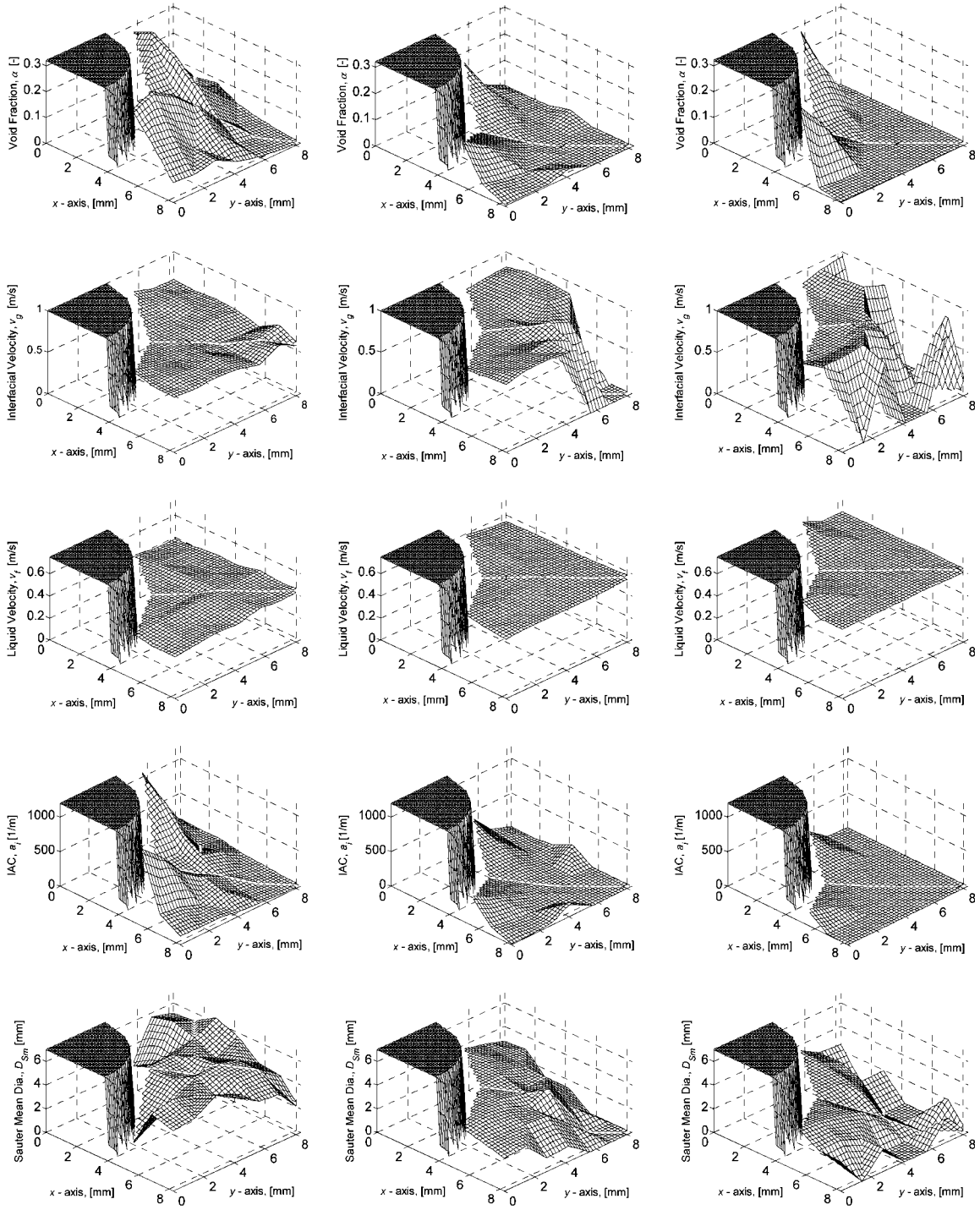

Fig. 4 Evolution of two-phase flow parameters with G. First column: $G = 354\,\mathrm{kg/m^2\,s}$, $q = 158\,\mathrm{kW/m^2}$, $T_{in} = 102.5^{\circ}\mathrm{C}$, $\Delta T_{sub} = 4.5^{\circ}\mathrm{C}$; second column: $G = 411\,\mathrm{kg/m^2\,s}$, $q = 158\,\mathrm{kW/m^2}$, $T_{in} = 103.2^{\circ}\mathrm{C}$, $\Delta T_{sub} = 3.7^{\circ}\mathrm{C}$; third column: $G = 513\,\mathrm{kg/m^2\,s}$, $q = 158\,\mathrm{kW/m^2}$, $T_{in} = 103.4^{\circ}\mathrm{C}$, $\Delta T_{sub} = 4.4^{\circ}\mathrm{C}$

of the interfacial velocity on the heat flux is more important for low liquid velocity values, but this fact can be explained since the range in the heat flux is wider for low liquid flow conditions (see Fig. 7). The increment in the v_g values with the heat flux is around 30% for the set of graphs that corresponds to the lowest G value. Figure 8 indicates that this increment is related to the increase in the liquid velocity near the rod due to the presence of bubbles. The influence of the heat flux on the interfacial velocity is much weaker for high liquid velocity values, since under these flow conditions, the v_g values are mainly determined by the liquid velocity. Finally, the Sauter mean diameter of the bubbles is increased with the heat flux (see Fig. 9). For low q values, the maximum D_{Sm} is near the rod; however, when the heat is incremented, the D_{Sm} shows a maximum in the center of the subchannel. The influence of the heat flux on the local flow parameters in the rod bundle geometry shows a trend similar to that observed for the annulus geometry of similar hydraul-

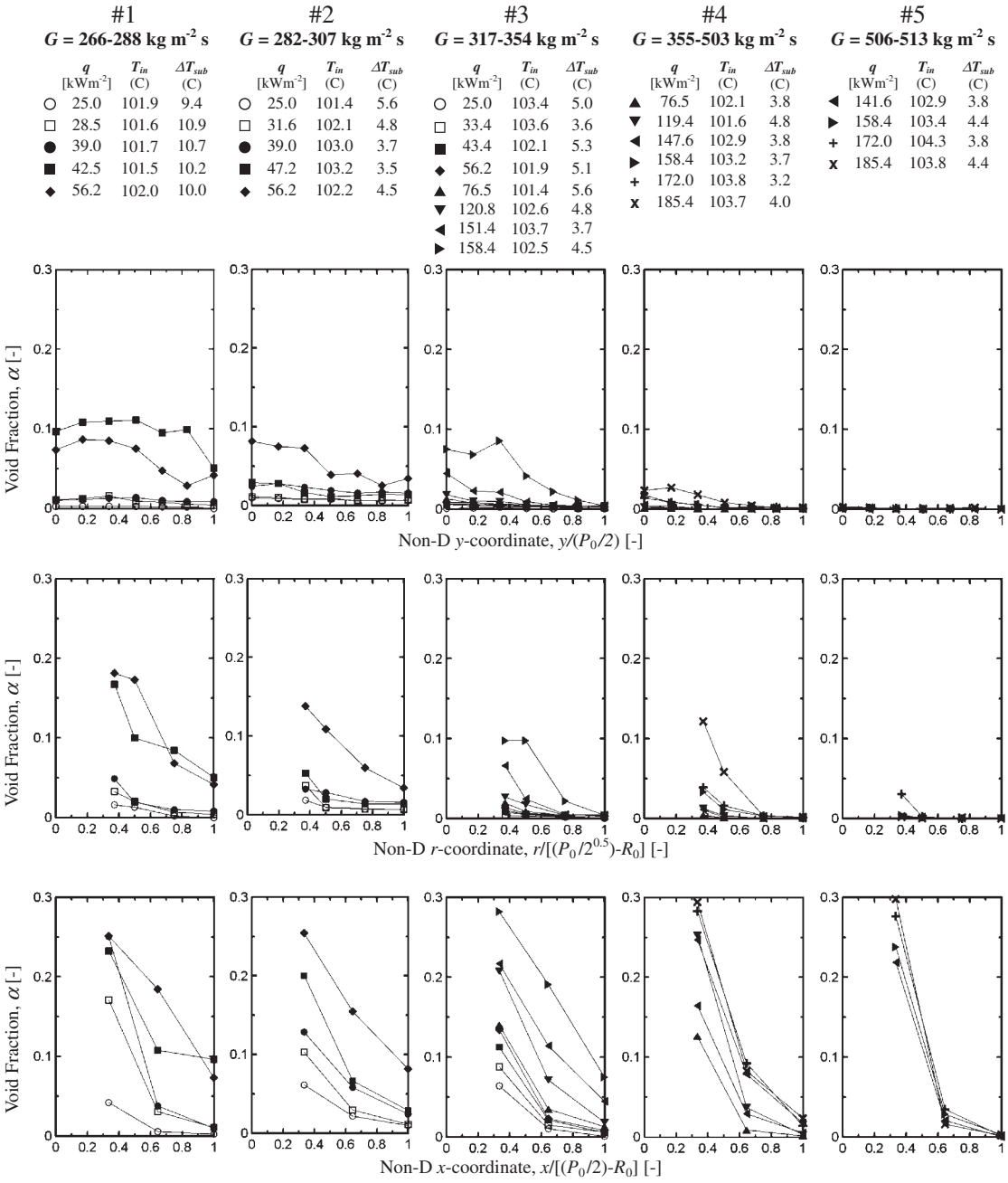

Fig. 5 Local void fraction profiles

ic diameter.[5,6] In general, an increment in the mass flux produces an effect opposite to that of the increment in the heat flux.

2. Area-Averaged Flow Parameters

In order to validate the drift-flux models and interfacial area concentration correlations described in Section II, the local data needs to be integrated to obtain area-averaged flow parameters. In addition, the measurement was not performed in the subchannel area near the rod surface because the finite size of the local probes needs to be taken into account. Thus, the local flow data in the rod surface needs to be assumed in order to be interpolated with the existing data points closest to the rod. In this study, different options have been considered for α, j, v_r, and a_i values near the heater rod. As can be seen in Eq. (2), the j and α are needed for the distribution parameter calculation, the v_r for the drift velocity calculation, and the a_i for the interfacial area concentration calculation. It should be noted here that the bubble interfacial velocity is approximately the same as the gas velocity in the bubbly flow regime.[33]

For α and a_i, the values at the rod surface are assumed to be the same as those at the point closest to the rod surface multiplied by a factor ξ. The multiplying factor considered is within a range from 0 to 2. For j, since the liquid velocity at the rod surface is zero, only the gas velocity has to be considered. Then, we have two options as follows.

– The gas velocity at the rod surface is zero (zero-

Table 5 Flow conditions used in the local data graphs

		○	□	●	■	◆	▲	▼	◀	▶	+	×
Set	G [kg/m^2 s]	q [kW/m^2] T_{in} (C) ΔT_{sub} (C)	q [kW/m^2] T_{in} (C) ΔT_{sub} (C)	q [kW/m^2] T_{in} (C) ΔT_{sub} (C)	q [kW/m^2] T_{in} (C) ΔT_{sub} (C)	q [kW/m^2] T_{in} (C) ΔT_{sub} (C)	q [kW/m^2] T_{in} (C) ΔT_{sub} (C)	q [kW/m^2] T_{in} (C) ΔT_{sub} (C)	q'' [kW/m^2] T_{in} (C) ΔT_{sub} (C)	q'' [kW/m^2] T_{in} (C) ΔT_{sub} (C)	q [kW/m^2] T_{in} (C) ΔT_{sub} (C)	q [kW/m^2] T_{in} (C) ΔT_{sub} (C)
#1	266–288	25.0 101.9 9.4	28.5 101.6 10.9	39.0 101.7 10.7	42.5 101.5 10.2	56.2 102.0 10.0						
#2	282–307	25.0 101.4 5.6	31.6 102.1 4.8	39.0 103.0 3.7	47.2 103.2 3.5	56.2 102.2 4.5						
#3	317–354	25.0 103.4 5.0	33.4 103.6 3.6		43.4 102.1 5.3	56.2 101.9 5.1	76.5 101.4 5.6	120.8 102.6 4.8	151.4 103.7 3.7	158.4 102.5 4.5		
#4	355–503						76.5 102.1 3.8	119.4 101.6 4.8	147.6 102.9 3.8	158.4 103.2 3.7	172.0 103.8 3.2	185.4 103.7 4.0
#5	506–513								141.6 102.9 3.8	158.4 103.4 4.4	172.0 104.3 3.8	185.4 103.8 4.4

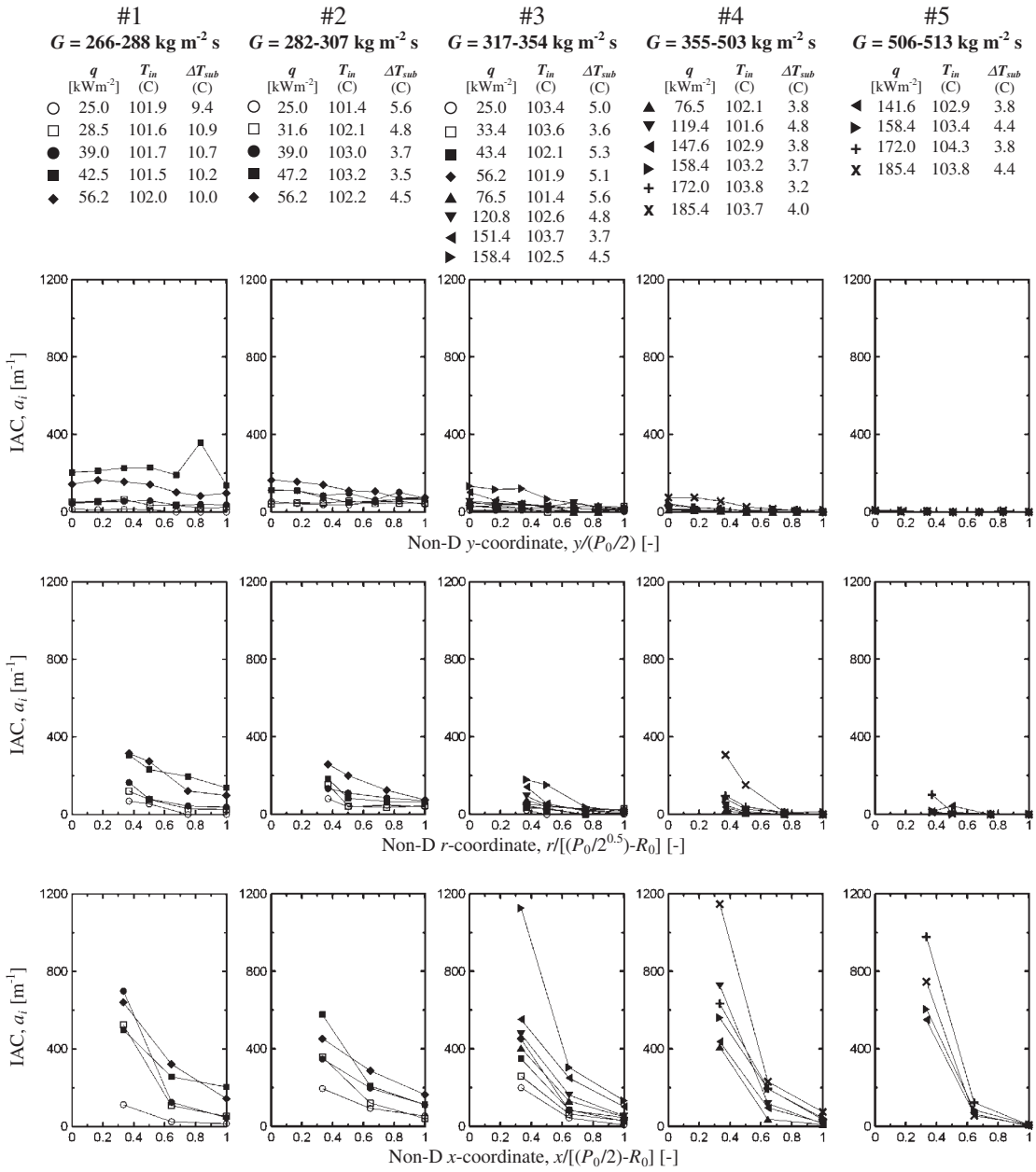

Fig. 6 Local interfacial area concentration profiles

mixture volumetric flux).

– The gas velocity at the rod surface is equal to the relative velocity and, in this case, the mixture volumetric flux is given as

$$j = v_r \alpha = \frac{\alpha}{1-\alpha} v_{gj}. \tag{7}$$

For v_r, two options are considered for the relative velocity as follows.

– The relative velocity at the rod surface is the same as that at the point closest to the rod surface.
– The relative velocity at the rod surface is zero.

All the options listed above and their possible combinations have been used for calculating the distribution parameter and drift velocity and the results have been compared with the existing correlations. This analysis shows that the reasonable option for v_r at the rod surface is the same relative velocity value as those at the point closest to the rod surface. This assumption is due to the fact that the relative velocity can be considered reasonably constant over the flow channel as reported by Serizawa *et al.*[34)]

The influence of the multiplying parameter ξ on the area-averaged void fraction and distribution parameters are shown in **Figs. 10**a and 10b, respectively. The effect of ξ on the area-averaged void fraction may not be so significant, being more important for low G values where the effect can be as high as $\pm 25\%$ for a very conservative estimate such as $\xi = 1 \pm 1$ ($0 \leq \xi \leq 2$). This effect is not so marked when the distribution parameter is considered and the maximum deviation in the C_0 value is $\pm 4.5\%$ for $\xi = 1 \pm 1$ ($0 \leq \xi \leq 2$). A value of ξ has been set at unity for all the calculations performed in this study. Then, the maximum estimation errors

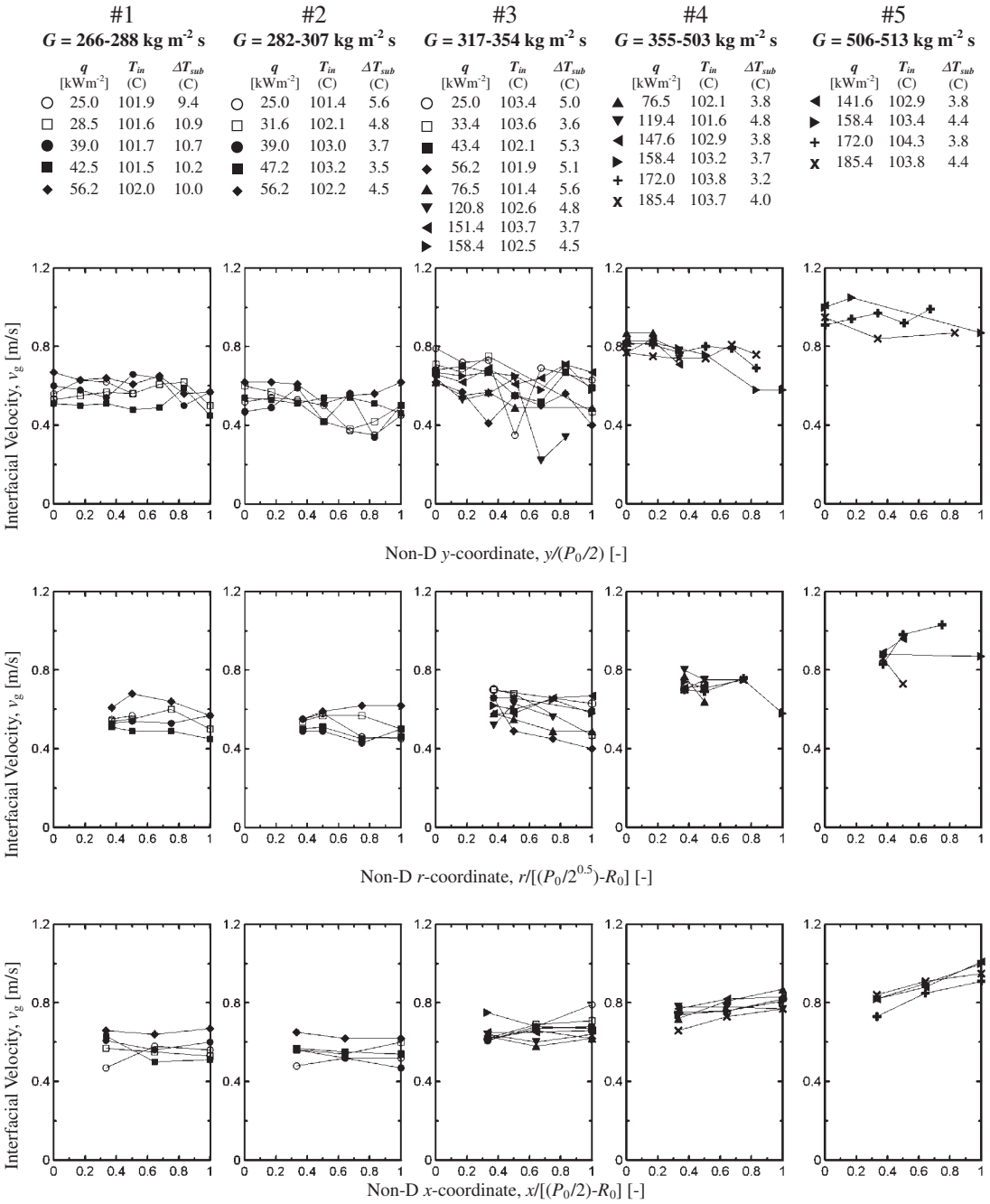

Fig. 7 Local interfacial velocity profiles

due to the assumed values at the heater rod are estimated to be ±25% and ±4.5% for $\langle\alpha\rangle$ (and $\langle a_i\rangle$) and C_0, respectively. The one-dimensional data obtained by integrating local data over the subchannel are shown in Table 4.

3. Comparison of Existing Drift-Flux Models with Data

The area-averaged results obtained by the integration of the local data have been used to check the prediction capabilities of the drift-flux models described in Section II in the rod bundle geometry. **Figures 11**a and 11b show the dependences of the distribution parameter and drift velocity values on the area-averaged void fraction, respectively. In addition, the predictions given using constitutive equations in the drift-flux models considered are shown in the same figures. For some of the models, a value of G is needed. In these cases, a value of G of 335 kg/m^2 s has been chosen, since it is the averaged value of the test matrix used in this study (see Table 4). This fact generates a source of error in the figures, but it is lower than 10% for all the flow conditions. Consequently, the information given in the figures should be taken for comparative purposes. The prediction error is defined as

$$E[\%] = \frac{|(\text{measured value}) - (\text{calculated value})|}{(\text{measured value})} \times 100. \quad (8)$$

Table 6 shows the averaged prediction errors of the constitutive equations of the distribution parameter and drift velocity listed in Table 1 as well as that of the area-averaged

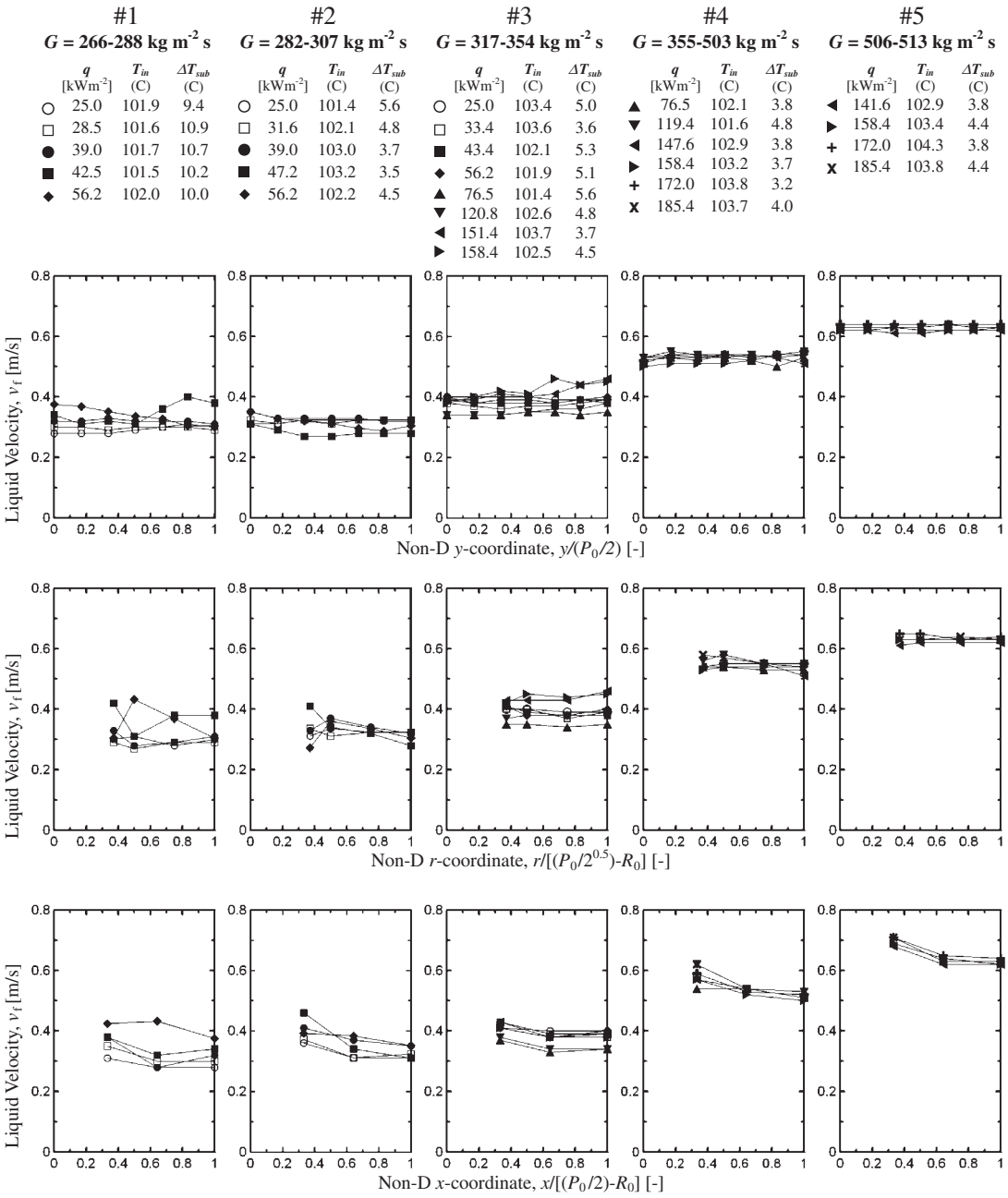

Fig. 8 Local liquid velocity profiles

void fraction using the constitutive equations and Eq. (1). Here, we assume that the constitutive equations obtained in rod bundles can be applicable to a subchannel, since the area of corner subchannels is much smaller than core subchannels of rod bundles in the experimental facilities that were used for obtaining the correlations (see Table 3).

As shown in Fig. 11a, the distribution parameter values in the tested conditions are always lower than 1, which corresponds to the typical wall-peaked void fraction profile present in subcooled boiling flow.[35] The distribution parameter is about 0.8 at $\langle\alpha\rangle = 0.02$ and gradually increases with $\langle\alpha\rangle$. Since the distribution parameter is zero at $\langle\alpha\rangle = 0$[20,35] in subcooled boiling flow, a very rapid increase in the distribution parameter is expected at $\langle\alpha\rangle < 0.02$. The extrapolation of the distribution parameter at higher $\langle\alpha\rangle$ implies the distribution parameter lower than 1.2. In Fig. 11a, the distribution parameters for round pipe[20] and internally heated annulus[15] are indicated by solid and dotted lines, respectively. In comparison with other channel geometries, the rapid C_0 increase in the subchannel occurs at lower $\langle\alpha\rangle$ due to the channel geometry effect. Here, we have developed an empirical correlation for a subchannel based on Ishii's approach[20] as

$$C_0 = \left(1.05 - 0.05\sqrt{\frac{\rho_g}{\rho_f}}\right)(1 - e^{-2.92\langle\alpha\rangle^{0.146}}), \qquad (9)$$

which is valid within a mass flow rate, heat flux, inlet temperature, and subcooled temperature ranges of 250–522 kg/m^2 s, 25–185 kW/m^2, 96.6–104.9°C, and 2–11 K, respectively. The thick solid line in Fig. 11a indicates the cal-

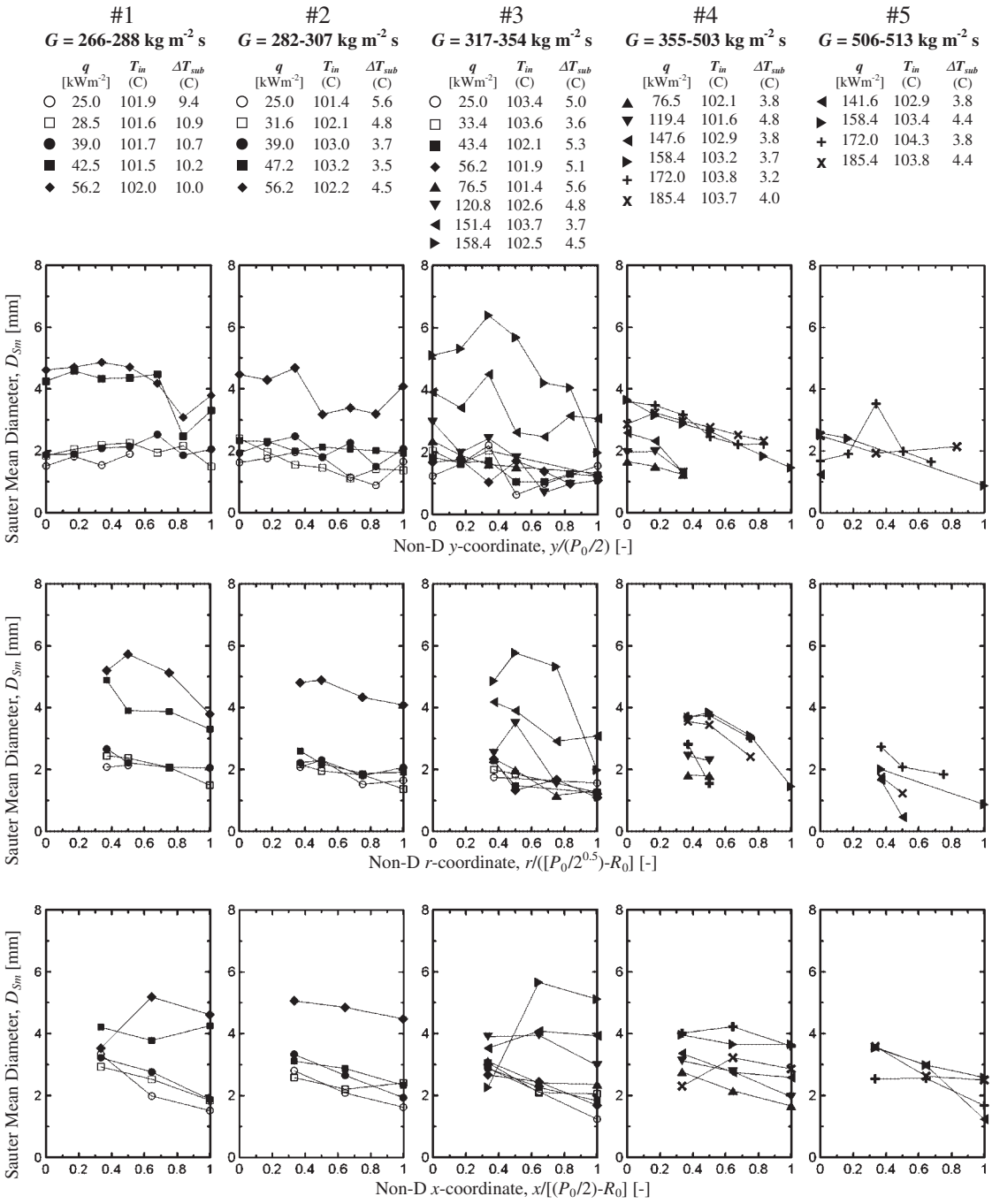

Fig. 9 Local Sauter mean diameter profiles

culation line using Eq. (9). The constitutive equations by Bestion, Inoue *et al.*, and Maier and Coddington tend to overestimate the distribution parameter and may not give a physically sound C_0 value at $\langle\alpha\rangle \to 0$. From a detailed comparison, the constitutive equation by Chexal *et al.* does not give reasonable predictions for the data obtained in this study. Nevertheless, the existing correlations give fairly good predictions for C_0 within an averaged relative deviation of 25% in an overall sense.

As shown in Fig. 11b, the void fraction weighted-averaged drift velocity shows a slight decrease with the void fraction as previously reported under bubbly flow conditions.[20,35] All the drift velocity constitutive equations that are based on the Zuber-Findlay expression (Chexal *et al.*,[12] Inoue *et al.*,[13] and Ishii[20]) also show this dependence. The Bestion equation[11] shows no appreciable dependence of the drift velocity on the void fraction, but the predicted values are close to the experimental ones and, thus, the average relative prediction error is 23.3%. The constitutive equations of Chexal *et al.*[12] and Inoue *et al.*[13] overestimate and underestimate systematically the drift velocity values, and the average relative prediction errors are 69.9% and 95.4%, respectively. The constitutive equation of Maier and Coddington[14] provides very high drift velocity values and the average prediction error is also very significant. These large discrepancies were also observed in the original

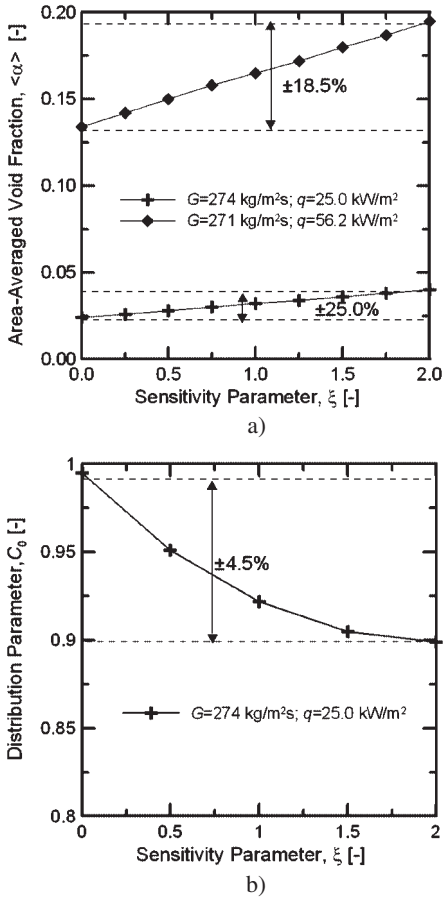

Fig. 10 Sensitivity analysis on effect of assumed void fraction at rod surface on a) area-averaged void fraction and b) distribution parameter

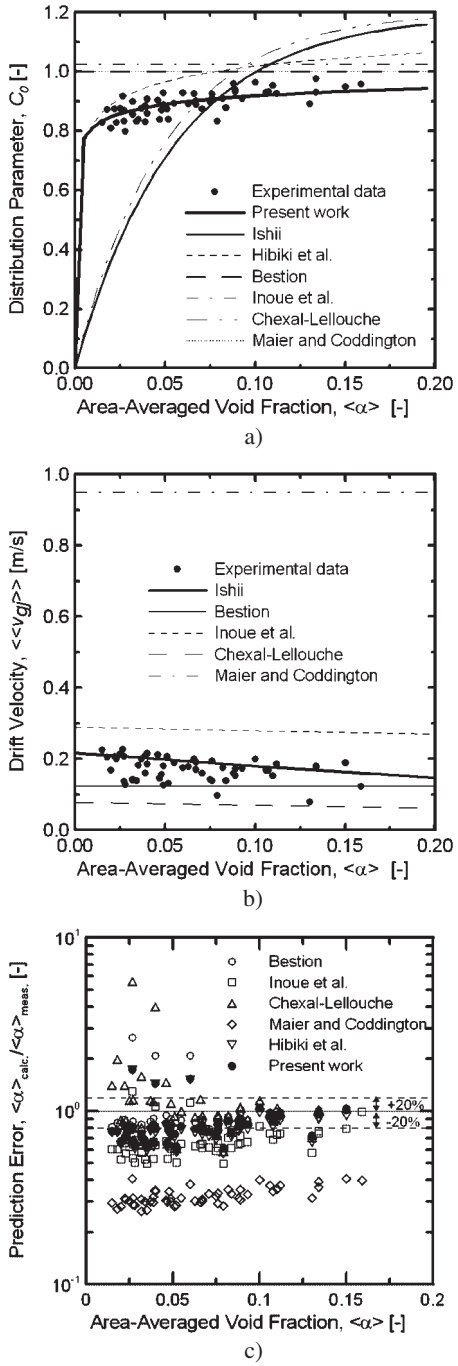

Fig. 11 Comparison of existing drift-flux models with data: a) distribution parameter, b) drift velocity, and c) void fraction

work of Maier and Coddington[14] for atmospheric pressure conditions. The lowest relative prediction error of 19.6% is given by Ishii.[20] The constitutive equation of the drift velocity by Ishii[20] also predicts the reasonable tendency of the drift velocity against the void fraction.

Concerning the area-averaged void fraction and as it is shown in Fig. 11c, all the correlations underestimate the void fraction values, except the one developed by Chexal *et al.* The lowest prediction error (±21.4%) is obtained using the distribution parameter given in Eq. (9) and the drift velocity proposed by Ishii.[20] In this case, the main part of the prediction error is given by the drift velocity value estimation. The prediction error can be reduced to ±2% if the estimated drift velocity value given by Ishii's equation is reduced by 20%. This fact can be supported by the rod walls effect on the bubble velocity. Considering an average bubble diameter of 5 mm and a hydraulic diameter of the subchannel of 36.2 mm, the existing correlations[36] predict a 10% to 20% reduction in the bubble velocity due to the walls effect. However, these correlations were developed for round pipes and their results need to be checked in more complex channel geometries such as rod bundles.

In all the correlations, the prediction accuracy is improved for increased area-averaged void fraction where the distribution parameter effect is more pronounced than the drift velocity effect. Among the existing correlations, the best results are obtained with the Bestion and Hibiki *et al.* (2003) correlations. The results obtained using the Bestion correlation are remarkable since it is a quite simple correlation that is applicable to the whole range of void fractions. However, the Bestion and Chexal *et al.* correlations present high scattering for low void fraction conditions. The predictions using Inoue *et al.* and Chexal *et al.* correlations are similar, providing area-averaged void fraction prediction errors lower than ±40%. The Maier and Coddington correlations do not provide reasonable predictions since the error in the drift velocity estimation is very high.

Table 6 Prediction accuracy of drift-flux models and interfacial area concentration correlations

Authors	Averaged error C_0	Averaged error $\langle\langle v_{gj}\rangle\rangle$	Averaged error $\langle\alpha\rangle$	Averaged error $\langle a_i\rangle$
Bestion (1990)	±12.3%	±23.3%	±23.8%	—
Inoue *et al.* (1993)	±15.3%	±95.4%	±35.1%	—
Chexal *et al.* (1992)	±23.3%	±68.9%	±38.6%	—
Maier and Coddington (1997)	±12.4%	±420%	±67.6%	—
Hibiki *et al.* (2003)	±9.0%	±19.6%	±26.9%	—
Present work	±2.7%	±19.6%	±21.4%	—
Zeitoun *et al.* (1994)	—	—	—	±36.5%
Hibiki and Ishii (2002) ($D_H = 18.6$ mm)	—	—	—	±36.9%
Hibiki and Ishii (2002) ($D_H = 34.6$ mm)	—	—	—	±49.7%
Hibiki *et al.* (2006) ($D_H = 18.6$ mm)	—	—	—	±12.2%
Hibiki *et al.* (2006) ($D_H = 34.6$ mm)				±22.9%
TRAC-PF1 (1993)	—	—	—	±49.8%
RELAP5 (1995)	—	—	—	±69.7%

4. Comparison of Existing Interfacial Area Concentration Models with Data

The area-averaged results obtained by the integration of the local data have been used to check the prediction capabilities of the interfacial area concentration correlations described in Section II in the rod bundle geometry. **Figure 12** shows the dependence of the interfacial area concentration on the area-averaged void fraction. In addition, the predictions given using the correlations considered in Section II are shown. Like in the previous section, for some of the correlations, a value of G is needed. In these cases, a value of G of 335 kg/m^2 s has been chosen. This fact generates a source of error in the figure, but it is lower than 10% for all the flow conditions. In addition, some of the existing correlations use the hydraulic diameter as an input. This fact can assume an additional source of error in rod bundle geometries since different hydraulic diameters can be defined. In the case of the Hibiki and Ishii (2002)[22] and Hibiki *et al.* (2006)[23] correlations, the hydraulic diameter value is needed for both the frictional pressure loss and Laplace length calculations. In Fig. 12, two different sets of results are given for the mentioned correlations; in all the cases, the whole rod bundle hydraulic diameter is considered for the frictional pressure loss calculation (since this effect affects the whole rod bundle). However, the whole bundle and subchannel hydraulic diameter values will be considered in the Laplace length calculation. Table 6 provides the averaged prediction errors calculated following Eq. (8).

As expected in the bubbly flow, the interfacial area concentration monotonically increases with the void fraction.

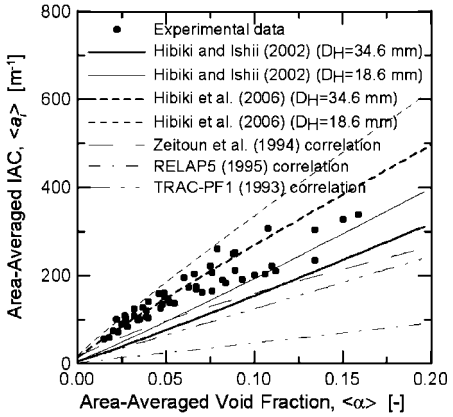

Fig. 12 Comparison of existing interfacial area concentration correlations with data

Almost all the considered correlations underestimate the interfacial area concentration in the subchannel of the 3 × 3 rod bundle geometry, even for very low average void fraction values. The correlations implemented in the TRAC-PF1[8] and RELAP5[9] thermal-hydraulic codes do not give reasonable predictions of the interfacial area concentration with the averaged relative errors of 49.8 and 69.7%, respectively. This fact is easily explained by the simplicity of these correlations. The correlation of Zeitoun *et al.*[21] provides the reasonable dependence of the interfacial area concentration on the area-averaged void fraction, but tends to underestimate the interfacial area concentration. The averaged relative prediction error is estimated to be 36.5%.

Hibiki and Ishii[22] developed the interfacial area correlation based on extensive data obtained at adiabatic conditions, and Hibiki *et al.*[23] modified it to extend the applicability to boiling flow. Both correlations have been employed using two different hydraulic diameters for the Laplace length calculation (considering the whole rod bundle and only the measured subchannel). The predictions given using the correlation developed by Hibiki and Ishii (2002) underestimate the interfacial area concentration results for both D_H values with averaged relative errors of 36.5% ($D_H = 18.6$ mm) and 49.7% ($D_H = 34.6$ mm). This discrepancy may be due to the assumptions and adiabatic flow databases utilized in the finalization of the correlation. The correlation given by Hibiki *et al.* (2006)[23] provides more accurate predictions. In this case, the use of the subchannel hydraulic diameter provides better results (±12.2%) than those obtained with the whole rod bundle hydraulic diameter (±22.9%). It is also possible to observe that the discrepancy between the correlation and the experimental data is enlarged with the averaged void fraction. In a previous work,[37] it was shown that the cap bubble formation can start at averaged void fraction values as low as 0.15. In the results shown in Fig. 9, Sauter mean diameter values larger than 6 mm can be found for high gas fractions. If these large bubbles are present in the subchannel, the correlations used in this work may overestimate the interfacial area values since they were developed for bubbly flow conditions.

V. Conclusions

The flow structure of subcooled boiling flow in a subchannel of 3 × 3 rod bundles is presented and analyzed. The local void fraction, interfacial area concentration, interfacial velocity, Sauter mean diameter, and liquid velocity have been measured using a conductivity probe and a Pitot tube in 20 locations inside one of the subchannels. A total of 53 flow conditions have been considered in the experimental dataset with atmospheric pressure conditions and a mass flow rate, heat flux, inlet temperature, and subcooled temperature ranges of 250–522 kg/m^2 s, 25–185 kW/m^2, 96.6–104.9°C, and 2–11 K respectively.

The influence of the heat flux on the local flow parameters in the rod bundle geometry shows a trend similar to that observed for the annulus geometry of similar hydraulic diameter. The increment in the heat flux in the rod with a constant mass flow rate produces an increment in the void fraction layer peak value and thickness around the rod surface. The interfacial area concentration profiles are similar to those of the void fraction. The increment in the interfacial velocity with the heat flux is only significant for low liquid velocity values. The Sauter mean diameter of the bubbles increases with the heat flux. An increment in the mass flux produces an effect opposite to that of the increment in the heat flux.

In addition, the area-averaged data integrated over the whole subchannel have been used to validate some of the distribution parameter and drift velocity constitutive equations and interfacial area concentration correlations most used in the literature as follows.

- Distribution parameter: The averaged relative prediction errors using existing correlations are lower than 25%. An empirical correlation is developed to predict the subchannel distribution parameter with an averaged relative prediction error of 2.7%.
- Drift velocity: The best prediction results are provided by Ishii's correlation with an averaged prediction error of 19.6%.
- Void fraction: The prediction errors provided using the existing correlations are lower than ±40% (except for the Maier and Coddington correlation) and the best results are obtained using the Bestion correlation with a prediction error of ±23.8%; however, this correlation presents major scattering for low void fraction conditions. By using the distribution parameter developed in this work and the drift velocity constitutive equation given by Ishii, it is possible to reduce the prediction error to ±21.4%. The prediction error can be reduced considerably if the estimated drift velocities are corrected by the wall effects.
- Interfacial area concentration: Most existing correlations underestimate the interfacial area concentration values and the best prediction results are obtained with the Hibiki *et al.* (2006) correlation developed for boiling flow. The use of the subchannel hydraulic diameter for the Laplece length calculations allows an averaged relative prediction error of 12.2% to be obtained.

Nomenclature

A: Cross-sectional area
a_i: Interfacial area concentration
C_0: Distribution parameter
D_0: Minimum bubble diameter
D_H: Hydraulic diameter
D_{Sm}: Sauter mean diameter
F: Quantity
G: Mass flow rate
j: Superficial velocity
Lo: Laplace length
N_{ai}: Dimensionless interfacial area concentration number
N_ρ: Density ratio number
p: Pressure
P_0: Pitch distance
q: Heat flux
Re: Reynolds number
R_{ef}: Liquid-phase Reynolds number
R_{eb}: Bubble Reynolds number
R_0: Rod radius
T: Temperature
v_g: Interfacial velocity
v_f: Liquid velocity
v_{gj}: Drift velocity
v_r: Relative velocity
Z: Axial distance

Greek symbols

α: Void fraction
ε: Energy dissipation rate per unit mass
υ: Kinematic viscosity
ρ: Density
σ: Surface tension

ξ: Sensitivity parameter

Subscripts

g: Gas phase
f: Liquid phase
in: Inlet
sub: Subcooled

Mathematical symbols

$\langle\ \rangle$: Area-averaged value
$\langle\langle\ \rangle\rangle$: Void fraction weighted cross-sectional area-averaged value

Acronyms

BWR: Boling Water Reactor
IAC: Interfacial Area Concentration
LSTF: Light Water High-Conversion Reactor
THTF: Thermal Hydraulic Test Facility
TPTF: Two-Phase Flow Test Facility

Acknowledgment

This study has been carried out under the nuclear R & D program supported by the Korean Ministry of Science and Technology. One of the authors (Yun) would like to express his sincere appreciation to Dr. C-.H. Song of the Korea Atomic Energy Research Institute for his continuous support and encouragement. The authors would like to express their special appreciation to Professor Mamoru Ishii of Purdue University for his fruitful discussions.

References

1) R. P. Roy, V. Velidandla, S. P. Kalra, P. Peturaud, "Local measurements in the two-phase region of turbulent subcooled boiling flow," *J. Heat Transfer-Trans. ASME* **116**[3], 660–669 (1994).
2) B. J. Yun, *Measurements of two-phase flow parameters in the subcooled boiling*, Ph. D. Thesis, Seoul National University, Korea (1996).
3) O. Zeitoun, M. Shoukri, "Bubble behaviour and mean diameter in subcooled boiling," *J. Heat Transfer-Trans. ASME* **118**[1], 110–116 (1996).
4) T. H. Lee, *A study on local two-phase flow structure of subcooled boiling in vertical and inclined annuli*, Ph. D. Thesis, Seoul National University, Korea (2000).
5) M. D. Bartel, M. Ishii, T. Masukawa, Y. Mi, R. Situ, "Interfacial area measurements in subcooled flow boiling," *Nucl. Eng. Des.* **210**[1–3], 135–155 (2001).
6) R. Situ, T. Hibiki, X. Sun, Y. Mi, M. Ishii, "Flow structure of subcooled boiling flow in an internally heated annulus," *Int. J. Heat and Mass Transfer* **47**[24], 5351–5364 (2004).
7) T. H. Lee, R. Situ, T. Hibiki, T. Takamasa, M. Ishii, "Axial development of subcooled boiling flow in a vertical concentric annulus," *Proc. 13th Int. Conf. on Nucl. Eng.*, ICONE13-50757 (2005).
8) J. W. Spore, S. J. Jolly-Woodruff, T. K. Knight, J.-C. Lin, R. A. Nelson, K. O. Pasamehmetoglu, R. G. Steinke, Ce. Unal, *TRAC-PF1/Mod2 Vol. I: Theory Manual, NUREG/CR-5673*, Nuclear Technology and Engineering Division, Los Alamos National Laboratory (1993).
9) The RELAP5 Code Development Team, *RELAP5/Mod3 Code Manual. Vol. IV: Models and Correlations, NUREG/CR-5535*, Idaho National Engineering Laboratory (1995).
10) N. Zuber, J. A. Findlay, "Average volumetric concentration in two-phase flow systems," *J. Heat Transfer* **87**[4], 453–468 (1965).
11) D. Bestion, "The physical closure laws in the CATHARE code," *Nucl. Eng. Des.* **124**[3], 229–245 (1990).
12) B. Chexal, G. Lellouche, J. Horowitz, J. Healzer, "A void fraction correlation for generalized applications," *Prog. Nucl. Ener.* **27**[4], 255–295 (1992).
13) A. Inoue, T. Kurosu, M. Yagi, S. Morooka, A. Hoshide, T. Ishizuka, K. Yoshimura, "In-bundle void measurement of a BWR fuel assembly by a X-ray CT scanner: assessment of BWR design void correlation and development of new void correlation," *Proc. ASME/JSME Nucl. Eng. Conf.* (1993).
14) D. Maier, P. Coddington, "Review of wide range void correlations against an extensive database of rod bundle void measurements," *Proc. of ICONE-5*, paper 2434 (1997).
15) T. Hibiki, R. Situ, Y. Mi, M. Ishii, "Modeling of bubble-layer thickness for formulation of one-dimensional interfacial area transport equation in subcooled boiling two-phase flow," *Int. J. Heat Mass Transfer* **46**[8], 1409–1423 (2003).
16) P. Coddington, R. Macian, "A study of the performance of void fraction correlations used in the context of drift-flux two-phase flow models," *Nucl. Eng. Des.* **215**[3], 199–216 (2002).
17) P. Venkateswararao, R. Semiat, A. E. Dukler, "Flow pattern transition for gas-liquid flow in a vertical rod bundle," *Int. J. Multiphase Flow* **8**[5], 509–524 (1982).
18) B. Chexal, G. Lellouche, *A Full Range Drift-Flux Correlation for Vertical Flows (Revison 1), EPRI report NP-3989-SR* (1986).
19) S. Morooka, A. Inoue, M. Oishi, T. Aoki, K. Nagaoka, H. Yoshida, "In-bundle void measurement of BWR fuel assembly by X-ray CT scanner," *Proc. ICONE-1*, Paper 38 (1991).
20) M. Ishii, *One-Dimensional Drift-Flux Model and Constitutive Equations for Relative Motion between Phases in Various Two-Phase Flow Regimes*, ANL-77-47, USA (1977).
21) O. Zeitoun, M. Shoukri, V. Chatoorgoon, "Measurement of interfacial area concentration in subcooled liquid-vapour flow," *Nucl. Eng. Des.* **152**[1–3], 243–255 (1994).
22) T. Hibiki, M. Ishii, "Interfacial area concentration of bubbly flow systems," *Chem. Eng. Sci.* **57**[18], 3967–3977 (2002).
23) T. Hibiki, T. H. Lee, J. Y. Lee, M. Ishii, "Interfacial area concentration in boiling bubbly flow systems," *Chem. Eng. Sci.* **61**[24], 7979–7990 (2006).
24) T. Mitsutake, S. Morooka, K. Suzuki, S. Tsunoyama, K. Yoshimura, "Void fraction estimation within rod bundles based on three-fluid model and comparison with X-ray CT void data," *Nucl. Eng. Des.* **120**[2–3], 203–212 (1990).
25) H. Kumamaru, M. Kondo, H. Murata, Y. Kukita, "Void-fraction distribution under high-pressure boil-off conditions in rod bundle geometry," *Nucl. Eng. Des.* **150**[1], 95–105 (1994).
26) R. Deruaz, P. Clement, J. M. Veteau, *Study of Two-Dimensional Effects in the Core of a Light Water Reactor during the ECC's Phase following a Loss of Coolant Accident*, EUR 10076 EN, Commissariat a l'Energie Atimique, Centre d'Etude Nucleaires de Grenoble, Service des Transferts Thermiques, Grenoble, (1985).
27) J. Dreier, G. Analytis, R. Chawla, "NEPTUN-III reflooding and boil-off experiments with an LWHCR fuel bundle simulator: experimental results and initial core assessment efforts," *Nucl. Tech.* **80**[1], 93–106 (1988).
28) Y. Anoda, Y. Kukita, K. Tasaka, "Void fraction distribution in rod bundle under high pressure conditions," *Proc. ASME Winter Annual Meeting, Advances in Gas-Liquid Flows* (1990).

29) T. M. Anklam, R. F. Miller, "Void fraction under high pressure, low flow conditions in rod bundle geometry," *Nucl. Eng. Des.* **75**[1], 99–108 (1983).
30) T. Hibiki, S. Hogsett, M. Ishii, "Local measurement of interfacial area, interfacial velocity and liquid turbulence in two-phase flow," *Nucl. Eng. Des.* **184**[2–3], 287–304 (1998).
31) T. Hibiki, M. Ishii, "Experimental study on interfacial area transport in bubbly two-phase flows," *Int. J. Heat Mass Transfer* **42**[16], 3019–3035 (1999).
32) H. A. Bosio, D. Malnes, "Water velocity measurements in air-water mixture," Euromech. Colloquium Mo, 7, Grenoble (1968).
33) T. Hibiki, M. Ishii, "One-group interfacial area transport of bubbly flows in vertical round tubes," *Int. J. Heat Mass Transfer* **43**[15], 2711–2726 (2000).
34) A. Serizawa, I. Kataoka, I. Michiyoshi, "Turbulence structure of air-water bubbly flow, I, II, and III," *Int. J. Multiphase Flow* **2**[3], 221–259 (1975).
35) T. Hibiki, M. Ishii, "Distribution parameter and drift velocity of drift-flux model in bubbly flow," *Int. J. Heat Mass Transfer* **45**[4], 707–721 (2002).
36) R. Clift, J. R. Grace, M. E. Weber, *Bubbles, Drops and Particles*, Academic Press, INC, New York, (1978).
37) T. Hibiki, M. Ishii, Z. Xiao, "Axial interfacial area transport of vertical bubbly flows," *Int. J. Heat Mass Transfer* **44**[10], 1869–1888 (2001).